Sustainable ammonia synthesis on TiO2-based photo-thermo catalysts

Laura Valenzuela, Javier Ivanez, Nicolas Keller

Sustainable ammonia synthesis on TiO_2-based photo-thermo catalysts

Laura Valenzuela, Javier Ivanez, Nicolas Keller*

Institut de Chimie et Procédés pour l'Energie, l'Environnement et la Santé (ICPEES), CNRS, Strasbourg University, 25 rue Becquerel, 67087, Strasbourg, France.

**Corresponding author:* nkeller@unistra.fr (N. Keller)

Abstract

The industrial production of ammonia (NH_3) by the Haber-Bosch process operates at high temperature and pressure, and remains highly energy-incentive. Hence, a sustainable strategy integrating sunlight as renewable energy input is a high-prospect alternative. We shows here the ability of Ru/TiO_2 and $Fe\text{-}TiO_2$ catalysts to benefit from a dual photonic/thermal excitation for boosting the NH_3 production rates from molecular N_2 and H_2 under UV-A light at ambient pressure. The synergistic effect evidenced allowed also to drive the synthesis of NH_3 at a lower temperature. The Ru/TiO_2 and $Fe\text{-}TiO_2$ photo-thermo catalysts were prepared by wet impregnation of a photoactive TiO_2 support, but differed in terms of structure and morphology. Ru/TiO_2 consisted in Ru nanoparticles (1.5 ± 0.3 nm) highly dispersed at the surface the TiO_2 support, while $Fe\text{-}TiO_2$ are described as a composite material formed by uniformly distributed submicrometric-scale aggregates of Fe and TiO_2 nanoparticles. The dual-mode excitation lowered the apparent activation energy from for Ru/TiO_2, while no significant change was observed for $Fe\text{-}TiO_2$, suggesting different light-induced reaction mechanisms. An optimum Fe content of 10 *wt.*% was observed, with the highest initial NH_3 production rate of 93 μmol g^{-1} h^{-1} at 350 °C under UV-A light that overcomes that achieved with Ru/TiO_2. In addition, the $Fe\text{-}TiO_2$ composite catalyst showed a better stability with time on stream than its Ru/TiO_2 counterpart that suffered from deactivation.

Keywords: Ammonia synthesis; Dual photonic/thermal excitation; Ru/TiO_2; Fe/TiO_2; Hot electrons; Light-to-heat delivery mechanism

1. Introduction

Ammonia (NH_3) is one of the main raw materials in the manufacture of basic organic chemicals and in the fertiliser industry, with a global production of approximately 185 Mt in 2021, according to the International Fertilizer Association (IFA) [1]. In addition, NH_3 has worth prospects as an alternative anergy carrier due to its carbon-free feature, large hydrogen capacity (17.6 *wt*.%), and being liquefiable (< 8 bar) [2, 3].

Currently, NH_3 is produced in the industry by the Haber-Bosch (H-B) process on an iron-based catalyst (primarily reduced magnetite ore, Fe_3O_4) operating at high temperature and pressure (350-500°C, 20-40 MPa). The synthesis of NH_3 mainly involves dissociative adsorption of the reactants ($*N_2 \rightarrow 2*N$ and $*H_2 \rightarrow 2*H$) and subsequent N-hydrogenation ($*NH_{(x-1)} + *H \rightleftharpoons *NH_x$; x = 1, 2, and 3), with nitrogen activation being the rate-limiting step owing to the extremely high bond energy of this molecule (945 kJ mol^{-1}) [4, 5]. The conversion of this catalytic process is thermodynamically limited, as the high temperature required kinetically by the nitrogen activation step reversely shifts the equilibrium towards NH_3 decomposition [6, 7]. Furthermore, in this process, nitrogen is obtained from the atmosphere by energy-intensive cryogenic separation, while hydrogen is generated *via* the combustion of carbon-based fuels [8]. Globally, the H-B process accounts for 1-2% of global energy consumption (more than 30 GJ/ton NH_3) and high greenhouse gas emissions (2.16 kgCO_2-eq/kg NH_3) [9].

Hence, the exploration of innovative and sustainable strategies to synthesize ammonia with the integration of sunlight as a renewable energy input is of emerging interest. Since Schrauzer and Guth first reported the nitrogen fixation by UV irradiation of TiO_2 under mild conditions [10], the photocatalytic production of NH_3 has been extensively described [11-14]. However, photocatalytic NH_3 synthesis generally involves gaseous N_2, liquid water and a solid catalyst, which poses problems related to the low solubility of N_2 in water and its limited diffusivity to the photocatalyst, leading to low NH_3 yields. Currently, photo-thermo catalysis is an innovative dual route that differs from the traditional single thermal or photocatalytic ones in the simultaneous use of photonic and thermal activation, where the heat can be obtained from an external source (conventional thermal reactors) or supplied by suited light absorption [15, 16]. Although photo-thermo catalysis is still in its infancy, it has been shown that it may simultaneously benefit from the high reaction rates associated with thermal activation and the increased selectivity of photonic processes, allowing catalytic reactions to take place under milder and more sustainable conditions. Photo-thermo catalytic synergies are usually reported to rely on specific electron-driven mechanisms and localised heat-delivery mechanisms that can occur simultaneous or separately [17, 18].

Dual photonic/thermal excitation of catalysts has evidenced synergy effects for NH_3 synthesis, allowing the reaction to proceed at lower temperatures and ambient pressure upon irradiation, while maintaining comparable conversion levels [6, 19-25]. Performing the reaction with gaseous N_2 and H_2 as reactants suppresses solubility and diffusivity limitations, and increases the process viability. However, catalyst engineering is challenging, and knowledge of the mechanisms under dual light/heat conditions remains limited. 3D graphene-hosted iron oxide was shown to activate N_2 to form NH_3 due to electron ejection from graphene using simulated sunlight without external heating [20,

23]. Peng et al. assigned to a localised heat mechanism the gas phase activity of a Cs-decorated $SrTiO_3$-supported Ru catalyst under vis/NIR irradiation [24]. Also, K/Ru/$TiO_{2-x}H_x$ (3 *wt*.% Ru) and $TiO_{2-x}H_y$/Fe exhibited highly efficient NH_3 synthesis rates under simulated sunlight, the support donated electrons to the active metals and accepted H atoms for successive N-hydrogenation, while localised heat favored N_2 activation at the metal surface, reaching apparent temperatures of 360 and 495 °C, respectively [6, 22]. The synergy of photo- and thermo-catalysis was shown using a Ni/TiO_2 catalyst (5-15 *wt*.% Ni), in which oxygen vacancies of TiO_2 accumulated photo-excited electrons and activated N_2, and Ni accommodated holes and dissociated H_2 [25].

In brief, the most common hybrid system in photo-thermo catalysis for NH_3 synthesis consists of an optically-responsive support, capable of absorbing light and promoting electrons to accelerate N_2 activation, and decorated with metal nanoparticles. In this context, TiO_2 stands out due to light absorbance ability, chemical stability and earth abundance. Regarding the supported metal, Fe and Ru are the conventional, most widely reported catalysts for NH_3 synthesis [26]. Therefore, the aim of this work was to study the ability of photoactive TiO_2 decorated with Fe and Ru to act as photo-thermo catalysts for NH_3 synthesis from molecular N_2 and H_2 under UV-A light. We demonstrated that the coupling of photonic and thermal excitations increased the NH_3 production rate for both Ru- and Fe-based TiO_2 catalysts, but different reaction mechanisms were suggested.

2. Materials and methods

2.1. Chemicals

Aeroxide® TiO_2 P25 was supplied by Evonik® (Evonik Resource Efficiency GmbH). Ruthenium (III) chloride hydrate ($RuCl_3$• xH_2O; 40 % Ru min. content), iron

(III) nitrate nonahydrate [$Fe(NO_3)_3$• $9H_2O$; ≥ 98 *wt*.%], sodium citrate tribasic dihydrate ($C_6H_5Na_3O_7$•$2H_2O$; ≥ 99 *wt*.%], sodium hydroxide (NaOH; ≥ 97 *wt*.%) and sulphuric acid (H_2SO_4; 95-97 *wt*.%) were obtained from Sigma-Aldrich. Sodium hypochlorite (NaOCl; 11-15% available chlorine), sodium pentacyanonitrosylferrate (III) dihydrate ($Na_2[Fe(CN)_5NO]$•$2H_2O$; ≥ 98 *wt*.%), salicylic acid ($C_7H_6O_3$; 99 *wt*.%) and ammonium chloride (NH_4Cl; ≥ 98 *wt*.%) were provided by ThermoFisher Scientific. Argon (Ar; ALPHAGAZ™ 1; ≥ 99.999 %) was purchased from Air Liquid. Hydrogen (H_2; ≥ 99.995 %) and nitrogen (N_2; 5.0 grade ≥ 99.999 %) were obtained from Linde France. All chemicals were used as received, without any further purification. Ultrapure water (18.2 MΩ•cm) was used in the preparation of solutions and catalysts.

2.2. Preparation of the photo-thermo catalysts

Ru/TiO_2 and $Fe\text{-}TiO_2$ catalysts were prepared by aqueous-phase wet impregnation using $RuCl_3$• xH_2O and $Fe(NO_3)_3$• $9H_2O$ as ruthenium and iron precursors, respectively, and Aeroxide ® TiO_2 P25 as support. Briefly, a certain amount of Ru or Fe precursors was dissolved in 15 mL water, and then 500 mg TiO_2 was dispersed in the solution by continuous stirring. After evaporation of the water at ambient temperature, the resulting solids were dried at 100°C for 1 h and subsequently subjected to a reductive treatment at 500 °C (5 °C min^{-1} heating rate) in H_2 flow for 1 h. Ru/TiO_2 was prepared with 5 *wt*.% ruthenium loading and denoted as $5Ru/TiO_2$. To better understand the mechanism of $Fe\text{-}TiO_2$, catalysts with 5, 10 and 20 *wt*.% iron loadings were investigated and named $5Fe\text{-}TiO_2$, $10Fe\text{-}TiO_2$ and $20Fe\text{-}TiO_2$, respectively.

2.3.Characterization techniques

Powder X-ray diffraction (XRD, Bruker D8-Advance diffractometer) analysis using Cu Kα radiation (λ = 1.54 Å) was performed to assess the crystal structure and crystallite size of the as-prepared catalysts by means of the Scherrer equation. Transmission electron microscopy (TEM) images of the 5Ru/TiO_2 catalyst were acquired in a JEOL 2100F microscope with a point resolution of 0.2 nm. The morphology and spatial distribution of the different phases in the Fe-TiO_2 photo-thermo catalysts were investigated by scanning electron microscopy (SEM) and energy dispersive X-ray spectroscopy (SEM-EDX, Zeiss Gemini SEM 500). The average particle size and size distribution of ruthenium and iron were obtained by analysing 300-400 particles using ImageJ software.

2.4. Photo-thermo catalytic experiments

Photo-thermo catalytic tests for NH_3 synthesis were conducted in a continuous-flow reactor consisting in a Harrick Scientific HVC-MRA 5 reaction chamber at ambient pressure. The H_2/N_2 (3/1, *v/v*) synthesis gas was flowed through the catalyst bed (surface density of 27 mg cm^{-2}) with a rate of 2.5 mL min^{-1} using Ar as carrier gas, with a total flow rate of 135 mL min^{-1}, corresponding to a WHSV of 1012.5 L g^{-1} h^{-1}. Flow rates were adjusted using Brooks® 5850 mass flow controllers. The catalyst was homogeneously heated to the reaction temperature within the 200-350 °C range using an external cartridge and a flowing water cooling system to accurately control the bulk temperature, and irradiated *via* a quartz window using a Thorlab M365LP1 LED (λ = 365 nm, 365 mW cm^{-2}). Prior to the start of each test, the inlet gas was analysed online by gas chromatography (R3000A gas microchromatograph, SRA instruments), allowing H_2 and N_2 quantification (MS 5A column) in the system. The gas-phase effluent was continuously bubbled into a customized absorption bottle containing a 2.5 mM H_2SO_4 aqueous solution (150 mL) to capture the NH_3 produced, which was sampled at regular

time-interval during the catalytic experiment (240 min). The experimental setup is schematically shown in Fig. S1.

The NH_3 concentration was analysed by the indophenol blue method using UV-vis spectrophotometry (UV-1600 PC, VWR) [20, 23, 27]. Specifically, 2 mL of aliquot from the absorption bottle was added to 500 µL of 1 M NaOH solution containing 5 *wt*.% salicylic acid and 5 *wt*.% sodium citrate, followed by the addition of 8 mL of ultrapure water, 100 µL of NaClO solution (4.5 *wt*.%) and 100 µL of $Na_2[Fe(CN)_5NO]•2H_2O$ solution (1 *wt*.%). After 1 h at room temperature, the formation of indophenol blue was determined using the absorbance at 700 nm. Absolute calibration of the method was obtained using NH_4Cl standard solutions and is shown in Fig. S2. The apparent activation energy (E_a) was calculated by linear fitting of the reaction data ln *r* (*r* in µmol g^{-1} h^{-1}) to $1/T$ (*T* in K) with least squares method in the range 200-350 °C according to the Arrhenius equation.

The catalytic results shown correspond to the average values of NH_3 production with error bars of ± 5%, obtained by duplicating the catalytic tests. Blank and controlled experiments performed in the absence of catalyst, under H_2/Ar flow in the absence of N_2, as well using the pure TiO_2 P25 support, did not shown any production of NH_3 in both dark and light conditions regardless of the temperature.

3. Results and discussion

3.1. Characterisation of the photo-thermo catalysts

The crystal structure of the photo-thermo catalysts was investigated by XRD (Fig. 1 and Table 1). The patterns for all catalysts displayed the diffraction peaks characteristic of both anatase (JCPDS 00-021-1272) and rutile (JCPDS 01-073-1765) TiO_2 phases of the Aeroxide ® TiO_2 P25 support, with their respective most intense (101) and (110)

planes at 2θ = 25.3° and 2θ = 27.5°, respectively, and with classical mean crystallite sizes of 22 ± 1 and 30 ± 1 nm, respectively. The catalysts displayed a phase composition with an anatase content of 81-82%, except for the Fe-TiO_2 catalysts for which the rutile content increased to 33-39% (*i.e.*, only 61-67% of anatase).

No Ru-related diffraction peaks were detected for the 5Ru/TiO_2 catalyst probably due to the small size of Ru nanoparticles and their homogeneous distribution on the TiO_2 surface [28]. By contrast, the XRD patterns recorded on Fe-TiO_2 materials exhibited additional reflexes at 2θ = 44.7, 65.0 and 82.3°, attributed to the (110), (200) and (211) planes of cubic iron (*Im3m* space group), respectively (JCPDS 00-006-0696). The intensity of the (110) diffraction peak related to Fe increased linearly with increasing the Fe content, while the mean crystallite size of Fe remained almost unchanged at 36-39 nm. A small decrease in the anatase/rutile ratio was observed for Fe-TiO_2 materials, that could result from an increase of the surface temperature that resulted from the exothermic decomposition of nitrates during the thermal reduction in H_2.

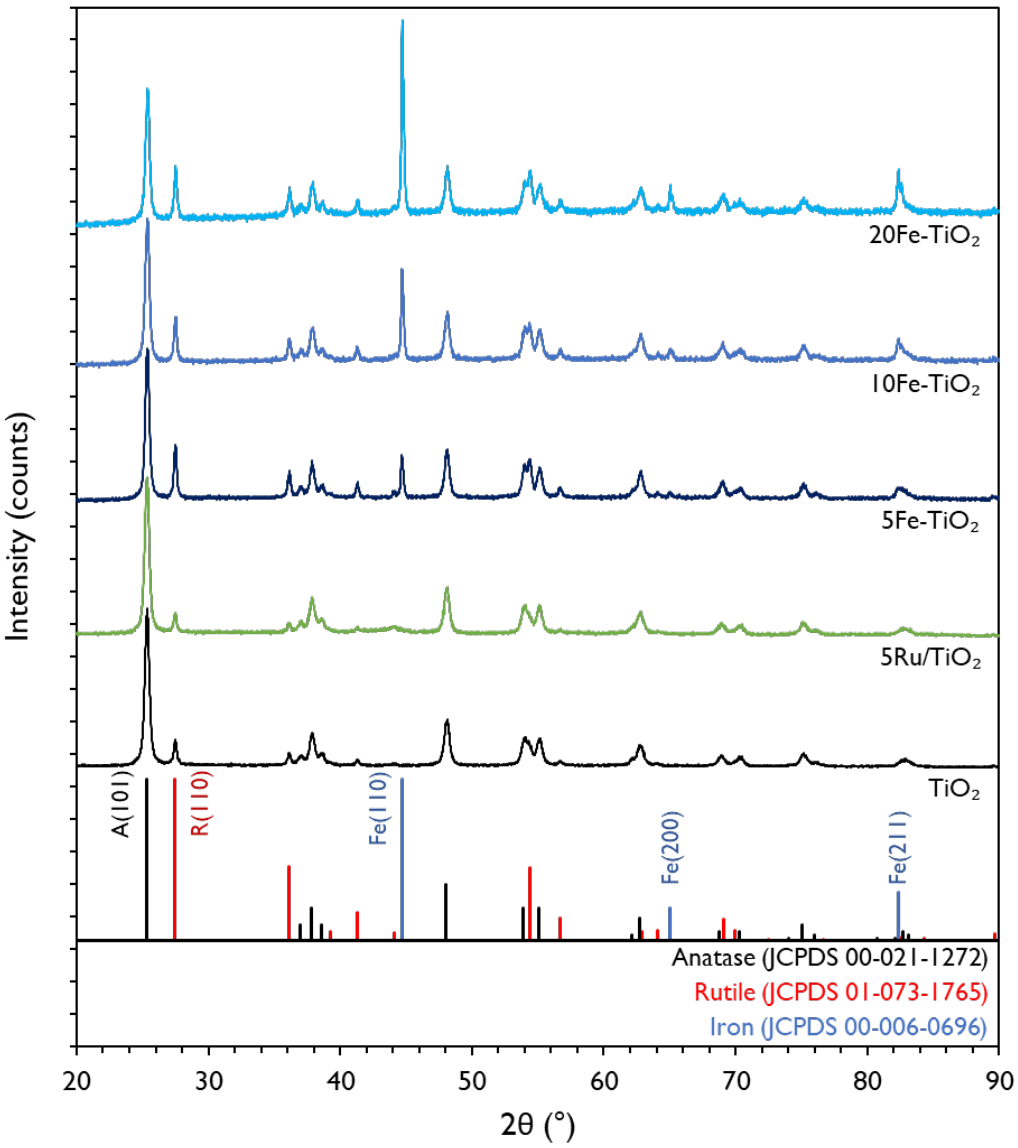

Figure 1. X-ray diffraction patterns of TiO_2 ■, 5Ru/TiO_2■, 5Fe-TiO_2■, 10Fe-TiO_2■ and 20Fe-TiO_2■.

Table 1. Mean crystallite sizes and anatase content derived from XRD data for TiO_2, 5Ru/TiO_2, 5Fe-TiO_2, 10Fe-TiO_2 and 20Fe-TiO_2 catalysts.

Catalyst	Mean crystallite size (nm)[a]			Crystallized phase composition, A/R (%)[b]	Normalized intensity of the Fe (110) peak [c]
	TiO_2 A(101)	TiO_2 R(110)	Fe (110)		
TiO_2	21	30	-	A: 81 – R: 19	-
5Ru/TiO_2	21	29	-	A: 82 – R: 18	-
5Fe-TiO_2	23	30	36	A: 66 – R: 34	1
10Fe-TiO_2	22	31	37	A: 67 – R: 33	2.14
20Fe-TiO_2	23	30	39	A: 61 – R: 39	4.16

[a] determined by applying the Scherrer equation to the most intense diffraction peak with the classical assumption of spherical crystallites.

[b] the composition corresponds to that within the crystallized TiO_2 phases (without considering the small content of amorphous TiO_2), calculated using the most intense reflexes of both anatase and rutile phases [29, 30].

[c] normalization is performed relative to the intensity of the Fe (110) peak.

TEM images of the 5Ru/TiO_2 catalyst shown in Fig. 2 revealed that Ru nanoparticles were highly dispersed on the TiO_2 surface, with no aggregate formation and an average particle size of 1.5 ± 0.3 nm. The metallic nature of the Ru nanoparticles was confirmed by lattice fringes with an interplane distance of 2.2 Å that corresponds to the (101) crystal planes of metallic Ru [31]. The morphology of the Fe-TiO_2 materials was studied by SEM-EDX, as displayed in Fig. 3. In addition to secondary electrons (SE), SEM images were also recorded using backscattered electrons detector (BSD) that provides high-contrast 2D images allowing an easy discrimination of Fe species and aggregates within the TiO_2 matrix samples with similar mean crystallite sizes. All the Fe-TiO_2 catalysts displayed a uniformly distributed pattern of nanoparticle aggregates of both TiO_2 and Fe phases with characteristic sizes in the submicron range. SEM images with BSD detector and elemental mappings revealed a homogeneous dispersion of Fe aggregates in the catalysts, the density of the aggregates increasing with the increase of the Fe content from 5 *wt.*% to 20 *wt.*%. Considering the accuracy of the measurements, both 5Fe- and 10Fe-TiO_2 catalysts displayed a similar mean size of Fe crystallite (nanoparticle) aggregates of 86 ± 23 and 71 ± 19 nm, respectively, while by far larger aggregates were observed for the 20Fe-TiO_2 catalyst (157 ± 39 nm). Thereby, both series of catalysts differ strongly in terms of structure and morphology, Ru/TiO_2 consisting of small size Ru nanoparticles decorating the TiO_2 support, while the Fe-TiO_2 catalysts can be consider as composite materials.

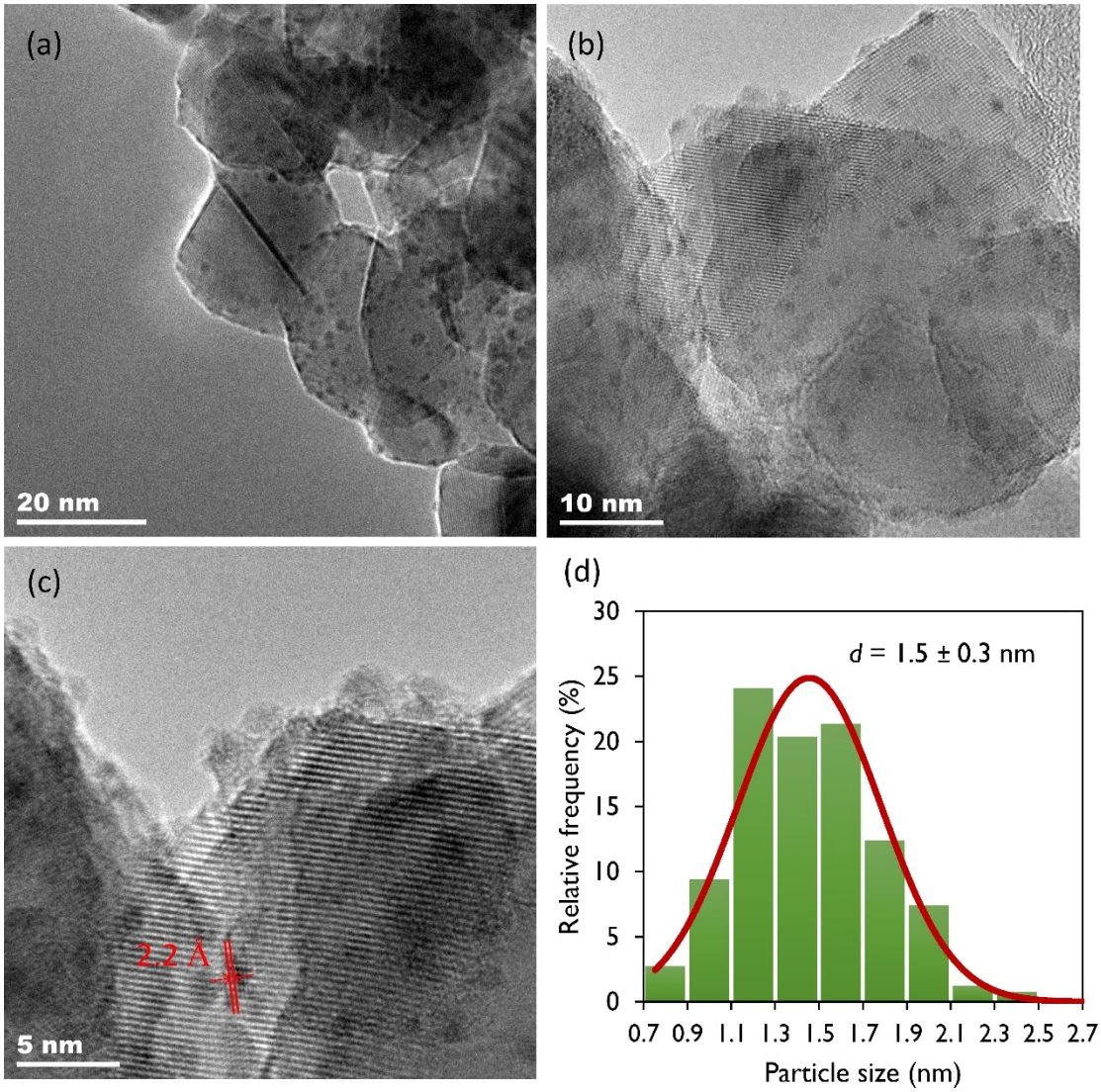

Figure 2. TEM images of the 5Ru/TiO_2 catalyst **(a-c)** and particle size distribution of Ru nanoparticles obtained from TEM images **(d)**.

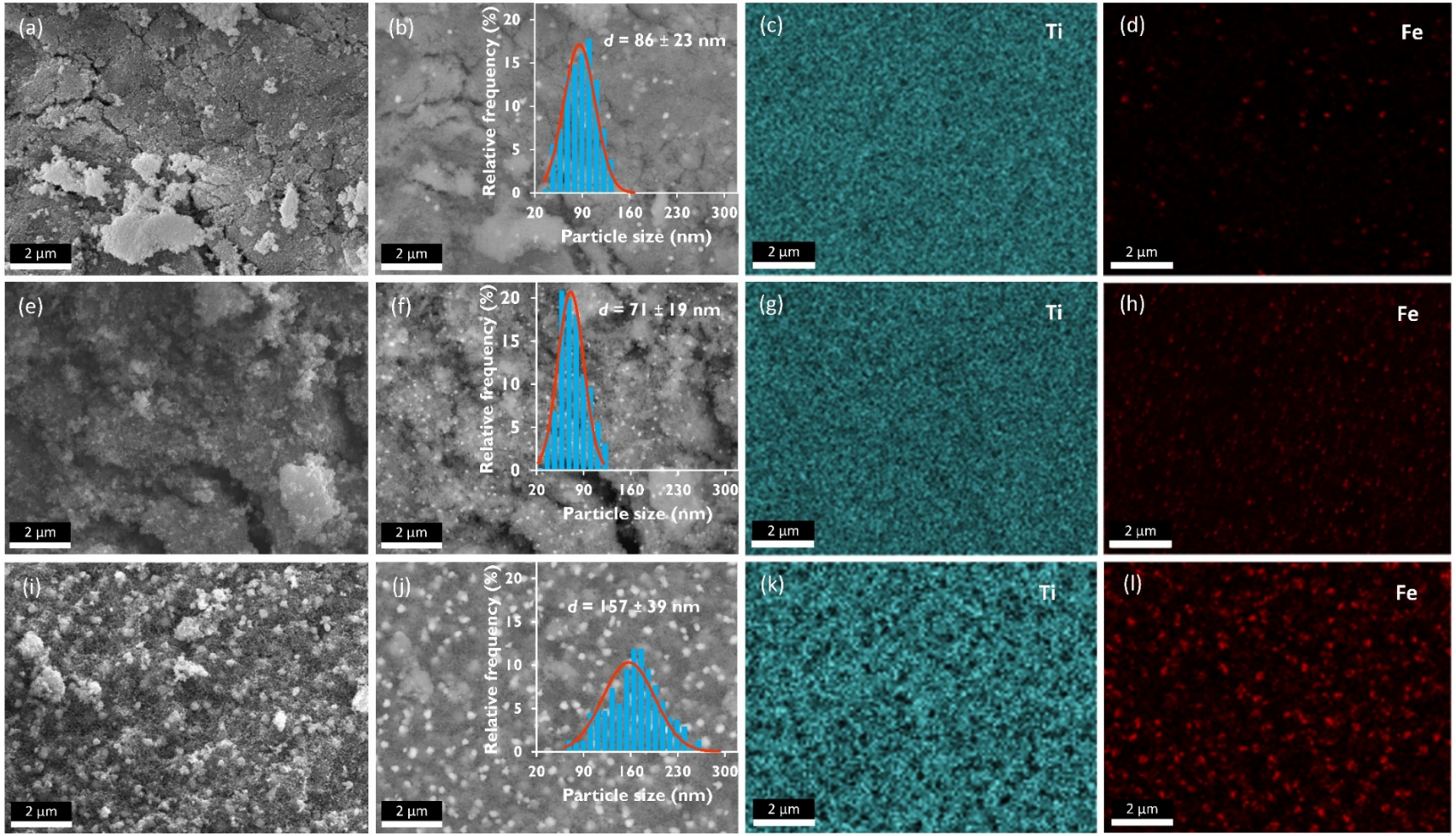
(a)
2 µm
(b)
Relative frequency (%)
d = 86 ± 23 nm
Particle size (nm)
(c)
Ti
(d)
Fe
(e)
(f)
d = 71 ± 19 nm
(g)
Ti
(h)
Fe
(i)
(j)
d = 157 ± 39 nm
(k)
Ti
(l)
Fe

Figure 3. SEM images obtained with SE **(a,e,i)** and BSD **(b,f,j)** detectors, size distribution of Fe particle aggregates **(insets of b,f,j images)** and SEM-EDX elemental mappings **(c-d, g-h, k-l)** of the 5 Fe-TiO_2 **(a-d)**, 10Fe-TiO_2 **(e-h)** and 20Fe-TiO_2 **(i-l)** catalysts. Ti: light blue (■); Fe: red (■).

3.2. Photo-thermo catalytic synthesis of NH_3

Fig. 4 depicts the performance of both 5Ru/TiO_2 and 5Fe-TiO_2 photo-thermo catalysts in the NH_3 synthesis under dark thermal and combined light/heat conditions over the 200-350 °C temperature range, expressed as the evolution of the concentration of NH_3 accumulated with the time on stream in the absorption bottle and as the initial NH_3 production rate. It was worth noticing that the dual photonic/thermal excitation increased the initial NH_3 production rate for both catalysts (Fig. 4 c-d). In the case of the 5Ru/TiO_2 catalyst, the initial NH_3 production rate increased 104% at the low temperature of 200°C, namely from 8 μmol g^{-1} h^{-1} to 16 μmol g^{-1} h^{-1}. The light-driven gain in NH_3 production rate appeared to be less pronounced with increasing the reaction temperature, decreasing to 44% at 250°C (from 14 μmol g^{-1} h^{-1} to 19 μmol g^{-1} h^{-1}) and 10% at 300°C (from 40 μmol g^{-1} h^{-1} to 44 μmol g^{-1} h^{-1}), down to a very low gain of 4% at 350°C (from 67 μmol g^{-1} h^{-1} to 69 μmol g^{-1} h^{-1}).

By contrast, the enhancement achieved by coupling photonic and thermal excitations using the 5Fe-TiO_2 material remained approximately constant over the investigated temperature range, with an average value of 15%. Indeed, the initial NH_3 production rate increased from 29 μmol g^{-1} h^{-1} to 36 μmol g^{-1} h^{-1} at the low temperature of 200°C, and from 39 μmol g^{-1} h^{-1} to 45 μmol g^{-1} h^{-1} at the higher temperature of 350°C. On both catalysts, dual-mode activation allowed similar NH_3 production rates to be achieved at lower temperatures, *i.e.* under milder conditions.

Both catalysts differ also in terms of their behavior with time on stream, as visualized in Fig. 4a,b and Fig. S3. In the plot of the time-evolution of the accumulated NH_3 concentration, the catalyst deactivation is characterized by the deviation to the slope at origin, that relates to the initial production rate. So, the 5Ru/TiO_2 catalyst deactivated on-stream relatively fast, the observed deactivation being all the more pronounced as the

temperature increases. No deactivation was observed only at the low temperature of 200°C. Conversely, the 5Fe-TiO_2 catalyst showed no deactivation on stream at 200-250 °C, the NH_3 production rate remaining constant for 4 h at 29 μmol g^{-1} h^{-1} in the dark and 36 μmol g^{-1} h^{-1} under light at 200°C, and at 39 μmol g^{-1} h^{-1} in the dark and 45 μmol g^{-1} h^{-1} under light at 250°C. Only very moderate deactivation was observed at higher temperature (Fig. 4b). The decrease in the NH_3 generation rate on 5Ru/TiO_2 could be attributed to the strong adsorption of H atoms that inhibit the dissociative adsorption of N_2 on the Ru surface [22, 32, 33]. The K/Ru/$TiO_{2-x}H_x$ catalyst developed by Mao et al. was proposed to overcome this limitation owing to the ability of the $TiO_{2-x}H_x$ support to reversibly accept H atoms from Ru and to deliver them to the activated N_2 to form Ti-NH_x (x = 1-3) under sunlight irradiation at room temperature and ambient pressure, keeping Ru free from H_2 poisoning [22]. Nevertheless, K/Ru/$TiO_{2-x}H_x$ reconstituted into K/Ru/TiO_2 after the reaction with its consequent deactivation, which was only recoverable by H_2 treatment at high temperatures. Interestingly, the reconstruction was reversible when the catalyst was subjected to a period of darkness after the reaction under solar irradiation conditions.

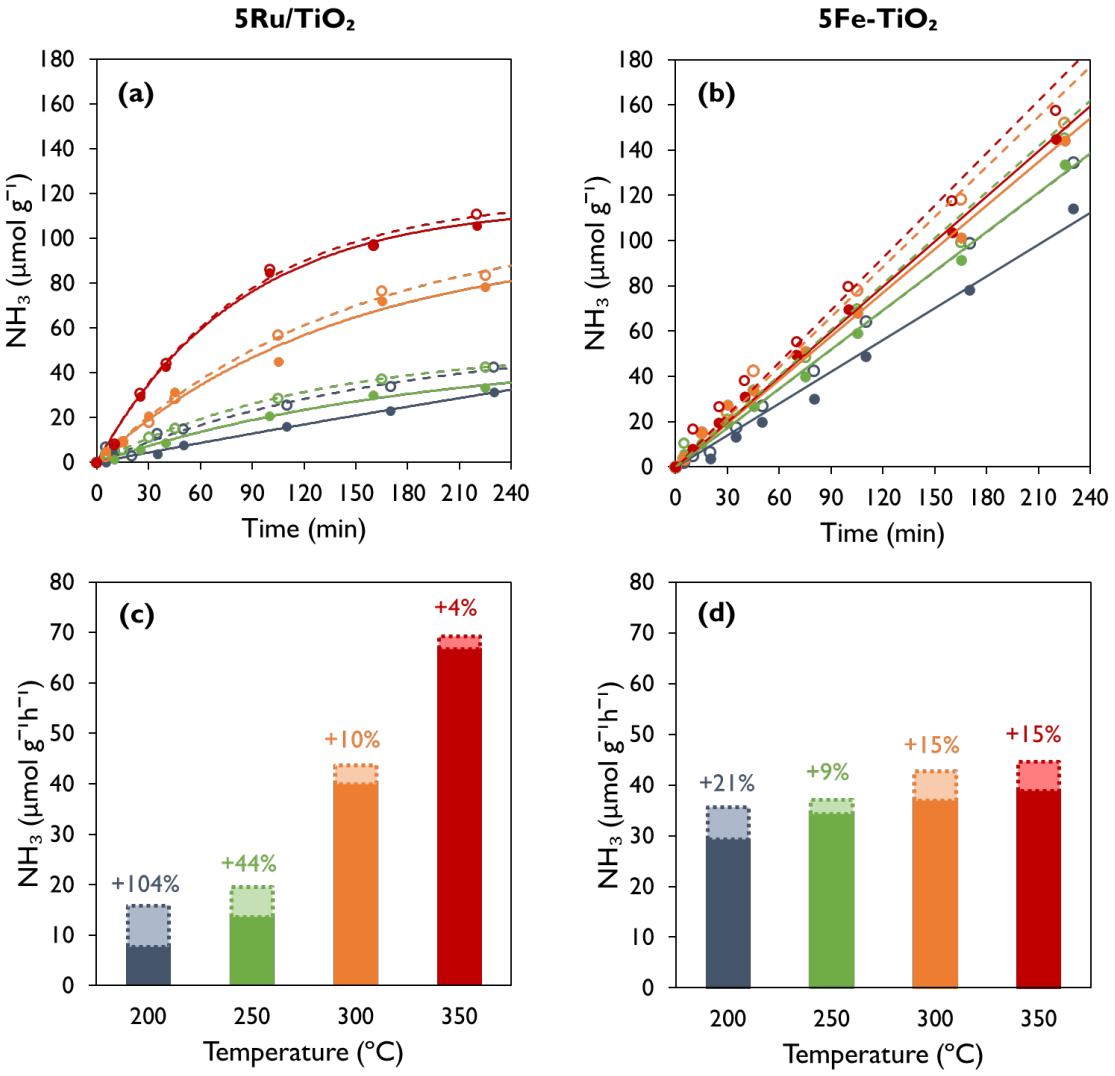

Figure 4. Time-evolution of the NH_3 concentration accumulated in the absorption bottle **(a-b)** and initial NH_3 production rate **(c-d)** obtained on the 5Ru/TiO_2 **(left)** and 5Fe-TiO_2 **(right)** catalysts, at ambient pressure in the temperature range 200-350 °C under dark thermal (—,●, ■) and dual light/heat (---, o, □) conditions. Temperatures: 200 °C (■), 250 °C (■), 300 °C (■) and 350 °C (■).

To highlight the superiority of photo-thermo catalysis over conventional thermal catalysis, the apparent activation energies were determined using the Arrhenius equation within the 200-350 °C temperature range, as shown in Fig. 5a. While both catalysts showed enhanced initial NH_3 production rate under combined photonic/thermal

excitation, it is worth noting that they strongly differ in the way the apparent activation energy of the reaction is impacted by the additional light irradiation. Both 5Ru/TiO_2 and 5Fe-TiO_2 catalysts displayed low apparent activation energies [34, 35]. However, on one hand, for the 5Ru/TiO_2 catalyst, the improved performance under dual light/heat conditions was accompanied by a decrease in the apparent activation energy from 37 kJ mol^{-1} to 25 kJ mol^{-1}, and the photo-thermo catalytic synthesis of NH_3 proceeded with a lower energy barrier than its pure thermal counterpart. On another hand, no significant change in the apparent activation energy (4 kJ mol^{-1}) occurred for the 5Fe-TiO_2 catalyst by combining photonic/thermal excitations. This may suggest a different reaction mechanism for both systems.

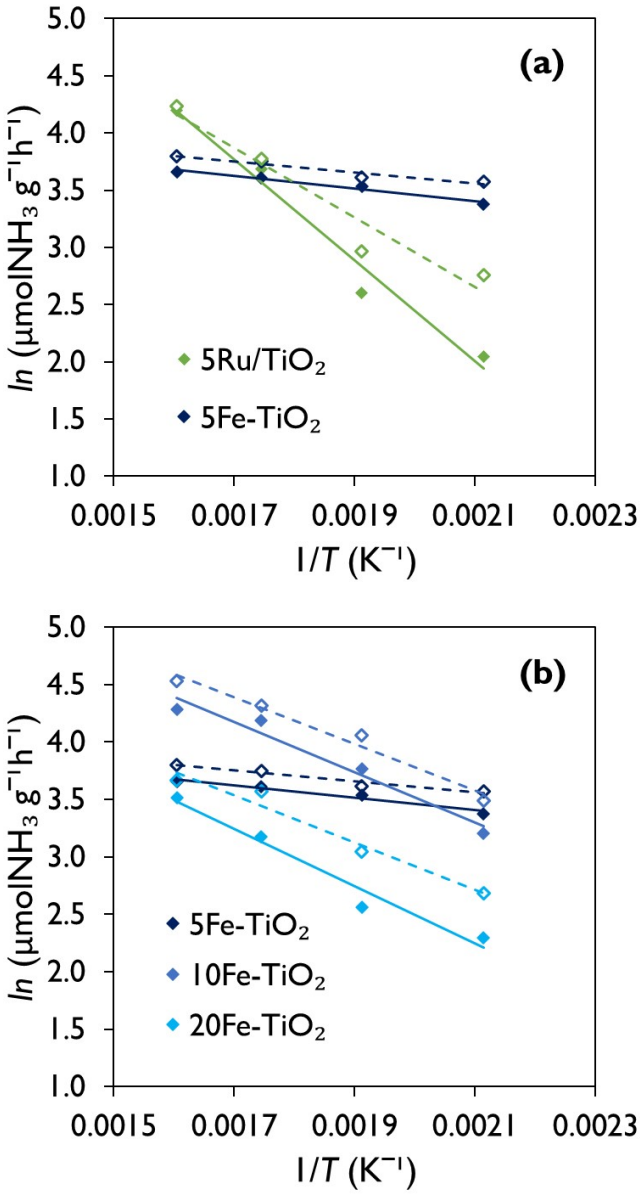

Figure 5. **(a)** Arrhenius plots for 5Ru/TiO_2 (◆) and 5Fe-TiO_2 (◆) at ambient pressure in the temperature range 200-350 °C under dark thermal (—,◆) and dual light/heat conditions (---,◇) ; **(b)** Influence of the Fe loading on the Arrhenius plots for the Fe-TiO_2 catalysts 5Fe-TiO_2 (◆), 10Fe-TiO_2 (◆) and 20Fe-TiO_2 (◆).

As the Fe-based TiO_2 catalyst outperformed the Ru/TiO_2 counterpart in terms of stability under the investigated experimental conditions, different Fe loadings (10 and 20 *wt.*%) were tested with the aim of increasing the NH_3 production rate. As can be observed in Fig. 6, the highest performances were observed for the 10Fe-TiO_2 photo-thermo catalyst, that reached under dark thermal conditions an initial NH_3 production rate of 66 $\mu mol\ g^{-1}\ h^{-1}$ and 72 $\mu mol\ g^{-1}\ h^{-1}$ at 300 °C and 350 °C, respectively, significantly higher (~2 times) than those achieved with the 5Fe-TiO_2 and 20Fe-TiO_2 counterparts. The NH_3 production rates of Fe-based catalysts are known to depend on the number of catalytic sites, which is influenced by Fe content, surface area and particle size [20, 36, 37]. As shown by XRD and SEM analyses, neither the size of Fe crystallites not that of aggregates were significantly impacted by the Fe content, except for the higher Fe content of 20 *wt.*%, for which strong agglomeration of Fe nanoparticles was observed. Thus, the higher activity of the 10Fe-TiO_2 catalyst might be related to a higher number of active sites compared to the 5Fe-TiO_2 catalyst, while the decrease in the number of active sites was detrimental to the activity of the 20Fe-TiO_2 catalyst.

Under dual photonic/thermal excitation, it was observed that the higher the Fe content in the catalyst, the greater the light-driven enhancement, with average values of enhancement of +15%, +27% and +44% for Fe contents 5 *wt.*%, 10 *wt.*% and 20 *wt.*%, respectively. It must be noted that a slight deactivation of the 10Fe-TiO_2 and 20Fe-TiO_2 catalysts was observed at the highest reaction temperatures and/or at a high NH_3 production rate, especially under combined light/heat conditions. This drop in catalytic activity might be attributed to heat-induced sintering and aggregation of Fe particles during the reaction [23, 37-39]. For this reason, the industrial H-B catalyst contains promoters (*e.g.*, alumina), which provide the catalyst with long-term stability [38, 39]. Fig. 5b depicts the Arrhenius plots for the Fe-based TiO_2 catalysts in the temperature

range from 200 to 350 °C. Similarly to the 5Fe-TiO_2 catalyst, no significant reduction in the apparent activation energy was observed using the Fe-TiO_2 catalysts with 10 and 20 *wt*.% Fe under combined photonic/thermal excitation compared to the dark thermal condition, suggesting in first approximation a similar reaction mechanism with increasing Fe content.

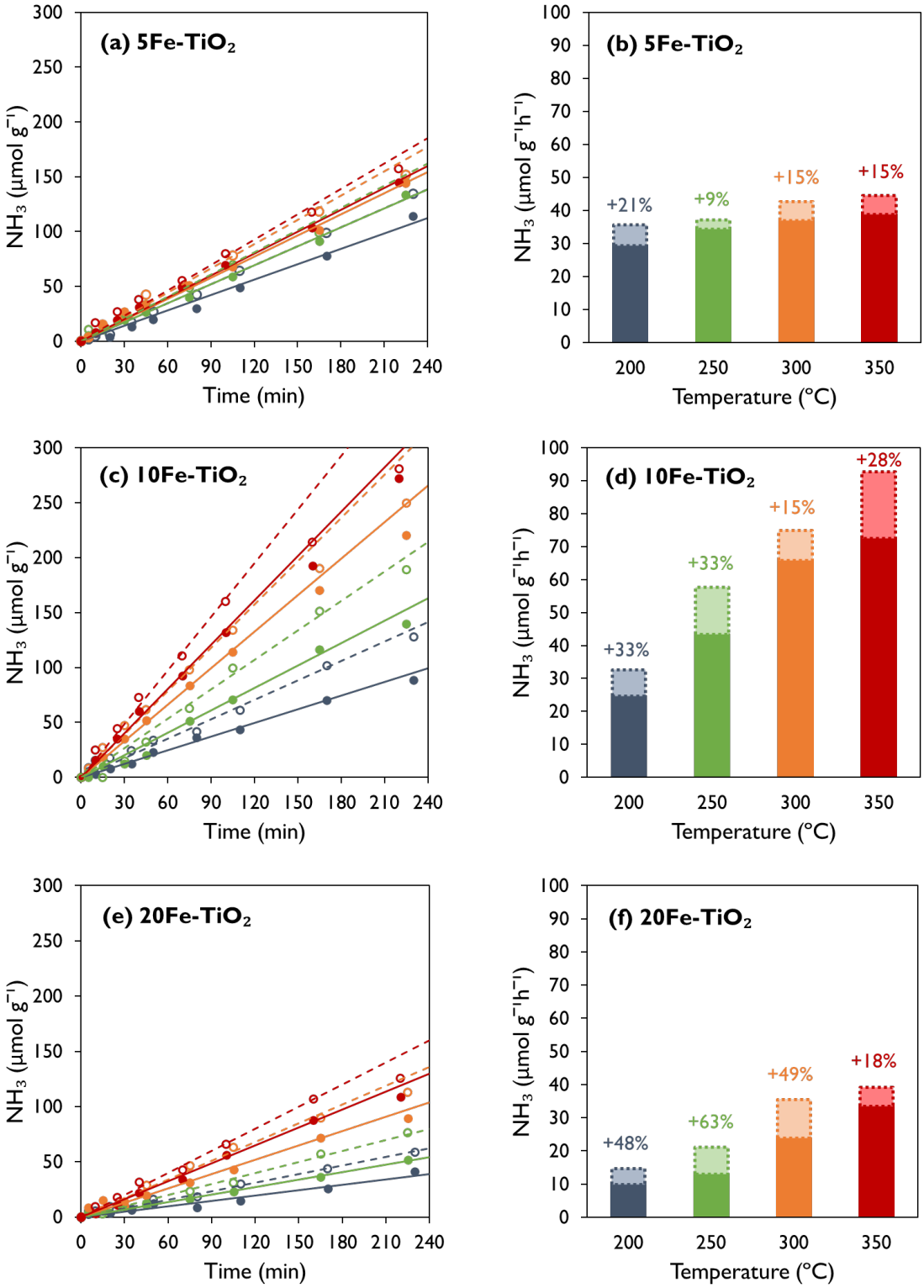

Figure 6. Time-evolution of the NH_3 concentration accumulated in the absorption bottle **(left)** and initial NH_3 production rate **(right)** obtained on the 10Fe-TiO_2 **(c-d)** and 20Fe-TiO_2 **(e-f)** catalysts, at ambient pressure in the temperature range 200-350 °C under dark

thermal (—,●, ■) and dual light/heat (---, o, □) conditions. Experiments performed using the 5Fe-TiO_2 catalyst **(a-b)** are also shown for comparison. Temperatures: 200 °C (■), 250 °C (■), 300 °C (■) and 350 °C (■).

The results suggest that the Ru/TiO_2 and Fe-TiO_2 catalysts operate through different reaction mechanisms under combined photonic/thermal excitation. The reduction of the energy barrier for 5Ru/TiO_2 under UV-A light irradiation might be mainly attributed to a photoelectron-driven mechanism. Indeed, although Ru nanoparticles are not regarded as plasmonic, they have been reported to significantly absorb UV and visible light with the formation of light-excited (hot) electrons from intra/interband transitions [19, 40-44]. The formation of hot electrons under UV-A light irradiation favors the reaction to proceed *via* a low-energy transition state, with the reduction of the apparent activation energy.

The role of excited electrons in Ru nanoparticles was already putted forward by Guo et al. to explain the performance of Ru/graphene in the photocatalytic Fischer-Tropsch synthesis [44], as well as by Ivanez et al. in the production of H_2 by gas-phase formic acid dehydrogenation on Ru/TiO_2 photo-thermo catalysts [45]. The generation of (excited) hot electrons in the metallic Ru could promote the N_2 dissociation, and the subsequent hydrogenation of $*NH_{(x-1)}$ into $*NH_x$ (x = 1, 2, 3) [19, 21, 44]. One hand hand Ru is proposed to accept the lone-pair electrons of N_2 to strengthen the metal-nitrogen bond, but it can also donate electrons to the antibonding orbitals of N_2 to weaken the N-N triple bond [28]. Apart from this mechanism, the transfer of the photogenerated electrons from the TiO_2 conduction band to Ru nanoparticles enhances the electron density at the Ru nanoparticles, what favors its surface reactivity. Meanwhile, due to the upward band bending caused by Ru deposition, the photogenerated holes will tend to migrate to the

semiconductor surface and be neutralized by H_2 promptly to form protons ($H_2 + 2h^+ \rightarrow 2H^+$) [28].

Conversely, the higher catalytic activity of Fe-TiO_2 catalysts under dual light/heat conditions obtained with no decrease in the apparent activation energy might be predominantly ascribed to a light-induced localised heat delivery mechanism [19, 46, 47], that involves the localised surface plasmon resonance states of Fe [6]. The light-to-heat conversion by plasmonic heating taking place on Fe nanoparticles might lead to a pronounced local temperature difference owing to the low thermal conductivity of TiO_2 (8.5 W/mK) compared to Fe (80 W/mK), so that the temperature of the Fe aggregates exceeds the average (bulk) temperature of the catalyst upon irradiation [48]. This mechanism was highlighted by Mao et al. in the case of metallic Fe nanonecklaces with 120 to 360 nm diameter size in contact with a low thermal conductivity $TiO_{2-x}H_y$ support, the temperature difference being quantified by the authors and shown to be size-dependent [6].

Mao et al. also indicated that an electron-driven mechanism could occur simultaneously to the plasmonic heating mechanism, with the injection of the hot electrons of the excited plasmonic Fe to unoccupied orbitals of adsorbed N_2 molecules *via* indirect and/or direct charge transfer. It should be noted that the interdependence of non-thermal (electron-driven) and thermal effects under photonic excitation makes the identification of the dominant mechanisms driving the reactions extremely difficult. So, we cannot not rule out the contribution to some (minor) extent of a mechanism involving the transfer of the photogenerated electron from TiO_2 to Fe where they would activate the adsorbed molecules, as proposed to occur between photo-excited graphene and Fe [20]. The contribution of each proposed mechanism, as well as the emergence of additional pathways, requires further investigation.

4. Conclusion

In this work we demonstrated that the ability of Ru/TiO_2 and $Fe\text{-}TiO_2$ catalysts to benefit from a dual-mode photonic/thermal excitation for the synthesis of NH_3 from molecular N_2 and H_2 under UV-A light. The Ru/TiO_2 and $Fe\text{-}TiO_2$ catalysts differed in terms of structure and morphology, the former consisting of Ru nanoparticles (1.5 ± 0.3 nm) homogeneously decorating the TiO_2 support and the latter being considered as a composite material with uniformly distributed nanoparticle aggregates of both TiO_2 and Fe phases with characteristic sizes in the sub-micron range. The combined photonic/thermal excitation boosted the NH_3 production rates for both types of catalysts at ambient pressure in the temperature range studied (200-350°C), and the dual-mode excitation allowed to drive the synthesis of NH_3 at a lower temperature.

The performance enhancement was accompanied by a decrease in the apparent activation energy from 37 KJ mol^{-1} to 25 KJ mol^{-1} for TiO_2 with 5 *wt*.% Ru, while it remained approximately constant for the $Fe\text{-}TiO_2$ composites. Therefore, different reaction mechanisms were suggested. A photoelectron-driven mechanism involving the light-excited (hot) electrons of metallic Ru was proposed for Ru/TiO_2. By contrast, a light-induced mechanism of localised heat delivery was suggested to prevail in $Fe\text{-}TiO_2$ composite catalysts. An optimum Fe content of 10 *wt.*% was observed, that led to the highest initial NH_3 production rate of 93 μmol g^{-1} h^{-1} at 350 °C under UV-A light, overcoming that achieved with the Ru/TiO_2 photo-thermo catalyst. In addition, the $Fe\text{-}TiO_2$ composite photo-thermo catalyst showed a better stability with time on stream than its Ru/TiO_2 counterpart that suffered from deactivation.

This work serves as a basis for the development of efficient photo-thermo catalytic processes able to synthesize renewable ammonia using solar energy.

Author Contributions

The manuscript was written through the contributions of all authors. All authors have given approval to the final version of the manuscript.

CRediT author statement

Laura Valenzuela Ávila: Methodology, Investigation, Formal analysis, Writing - original draft.

Javier Ivanez: Investigation, Formal analysis.

Nicolas Keller: Conceptualization, Funding acquisition, Methodology, Investigation, Formal analysis, Writing – original draft, Project administration, Supervision, Resources.

Declaration of Competing Interest

The authors declare no competing financial interest.

Data availability

Data will be made available on request.

Acknowledgements

Laura Valenzuela thanks the MOPGA program for her fellowship. The IdEx Program of the University of Strasbourg is acknowledged for funding the PhD fellowship of J. Ivanez. Dr. T. Dintzer (ICPEES) is thanked for performing SEM analysis.

References

[1] World ammonia statistics by region 2010-2021, International Fertilizer Association, (2023). https://www.ifastat.org/supply/Nitrogen%20Products/Ammonia

[2] W. Qiu, X.-Y. Xie, J. Qiu, W.-H. Fang, R. Liang, X. Ren, X. Ji, G. Cui, A.M. Asiri, G. Cui, B. Tang, X. Sun, High-performance artificial nitrogen fixation at ambient conditions using a metal-free electrocatalyst, Nat. Commun., 9 (2018) 3485. https://doi.org/10.1038/s41467-018-05758-5

[3] A. Valera-Medina, H. Xiao, M. Owen-Jones, W.I.F. David, P.J. Bowen, Ammonia for power, Prog. Energy Combust. Sci., 69 (2018) 63-102. https://doi.org/10.1016/j.pecs.2018.07.001

[4] K. Honkala, A. Hellman, I.N. Remediakis, A. Logadottir, A. Carlsson, S. Dahl, C.H. Christensen, J.K. Nørskov, Ammonia Synthesis from First-Principles Calculations, Science, 307 (2005) 555-558. https://doi.org/10.1126/science.1106435

[5] C.J.M. van der Ham, M.T.M. Koper, D.G.H. Hetterscheid, Challenges in reduction of dinitrogen by proton and electron transfer, Chem. Soc. Rev., 43 (2014) 5183-5191. https://doi.org/10.1039/C4CS00085D

[6] C. Mao, H. Li, H. Gu, J. Wang, Y. Zou, G. Qi, J. Xu, F. Deng, W. Shen, J. Li, S. Liu, J. Zhao, L. Zhang, Beyond the Thermal Equilibrium Limit of Ammonia Synthesis with Dual Temperature Zone Catalyst Powered by Solar Light, Chem, 5 (2019) 2702-2717. https://doi.org/10.1016/j.chempr.2019.07.021

[7] P. Wang, F. Chang, W. Gao, J. Guo, G. Wu, T. He, P. Chen, Breaking scaling relations to achieve low-temperature ammonia synthesis through LiH-mediated nitrogen transfer and hydrogenation, Nat. Chem., 9 (2017) 64-70. https://doi.org/10.1038/nchem.2595

[8] A.M.O. Mohamed, S.G. Al-Ghamdi, Y. Bicer, Life cycle assessment of clean ammonia synthesis from thermo-catalytic solar cracking of liquefied natural gas, Int. J. Hydrogen Energy., 46 (2021) 38551-38562. https://doi.org/10.1016/j.ijhydene.2021.09.080

[9] S. Ghavam, M. Vahdati, I.A.G. Wilson, P. Styring, Sustainable Ammonia Production Processes, Front. Energy Res., 9 (2021). https://doi.org/10.3389/fenrg.2021.580808

[10] G.N. Schrauzer, T.D. Guth, Photolysis of Water and Photoreduction of Nitrogen on Titanium Dioxide, J. Am. Chem. Soc., 99 (1977) 7189-7193. https://doi.org/10.1021/ja00464a015

[11] Z. Liu, S. Fan, X. Li, Z. Niu, J. Wang, C. Bai, J. Duan, M.O. Tadé, S. Liu, Synergistic effect of single-atom Cu and hierarchical polyhedron-like Ta3N5/CdIn2S4 S-scheme heterojunction for boosting photocatalytic NH3 synthesis, Appl. Catal. B: Environ., 327 (2023) 122416. https://doi.org/10.1016/j.apcatb.2023.122416

[12] T. Shan, H. Luo, S. Wu, J. Li, F. Zhang, H. Xiao, L. Huang, L. Chen, In situ formation of a covalent organic framework on g-C3N4 encapsulated with nanocellulosic carbon for enhanced photocatalytic N2-to-NH3 conversion, Fuel, 358 (2024) 130157. https://doi.org/10.1016/j.fuel.2023.130157

[13] D. Shi, Z. Shi, L. Zhang, Y. Cao, Enhanced photocatalytic NH3 synthesis for Bi2MoO6 regulated by doping of fluorine and iodine, J. Power Sources, 592 (2024) 233925. https://doi.org/10.1016/j.jpowsour.2023.233925

[14] J. Wang, L. Guan, S. Yuan, J. Zhang, C. Zhao, X. Hu, B. Teng, Y. Wu, Y. He, Greatly boosted photocatalytic N2-to-NH3 conversion by bismuth doping in CdMoO4: Band structure engineering and N2 adsorption modification, Sep. Purif. Technol., 314 (2023) 123554. https://doi.org/10.1016/j.seppur.2023.123554

[15] A. Iglesias-Juez, F. Fresno, J.M. Coronado, J. Highfield, A.M. Ruppert, N. Keller, Emerging high-prospect applications in photothermal catalysis, Curr. Opin. Green Sustain. Chem., 37 (2022) 100652. https://doi.org/10.1016/j.cogsc.2022.100652

[16] N. Keller, J. Ivanez, J. Highfield, A.M. Ruppert, Photo-/thermal synergies in heterogeneous catalysis: Towards low-temperature (solar-driven) processing for sustainable energy and chemicals, Appl. Catal. B: Environ., 296 (2021) 120320. https://doi.org/10.1016/j.apcatb.2021.120320

[17] M. Shi, X. Meng, Photothermal catalysis: From principles to applications, Int. J. Hydrogen Energy., 48 (2023) 34659-34676. https://doi.org/10.1016/j.ijhydene.2023.05.253

[18] Z. Wang, Z. Yang, R. Fang, Y. Yan, J. Ran, L. Zhang, A State-of-the-art review on action mechanism of photothermal catalytic reduction of CO2 in full solar spectrum, Chem. Eng. J., 429 (2022) 132322. https://doi.org/10.1016/j.cej.2021.132322

[19] X. Bian, Y. Zhao, G.I.N. Waterhouse, Y. Miao, C. Zhou, L.-Z. Wu, T. Zhang, Quantifying the Contribution of Hot Electrons in Photothermal Catalysis: A Case Study of Ammonia Synthesis over Carbon-supported Ru Catalyst, Angew. Chem., Int. Ed., 62 (2023) e202304452. https://doi.org/10.1002/anie.202304452

[20] Y. Lu, Y. Yang, T. Zhang, Z. Ge, H. Chang, P. Xiao, Y. Xie, L. Hua, Q. Li, H. Li, B. Ma, N. Guan, Y. Ma, Y. Chen, Photoprompted Hot Electrons from Bulk Cross-Linked Graphene Materials and Their Efficient Catalysis for Atmospheric Ammonia Synthesis, ACS Nano, 10 (2016) 10507-10515. https://doi.org/10.1021/acsnano.6b06472

[21] C. Mao, J. Wang, Y. Zou, G. Qi, J.Y. Yang Loh, T. Zhang, M. Xia, J. Xu, F. Deng, M. Ghoussoub, N.P. Kherani, L. Wang, H. Shang, M. Li, J. Li, X. Liu, Z. Ai, G.A. Ozin, J. Zhao, L. Zhang, Hydrogen Spillover to Oxygen Vacancy of TiO2–xHy/Fe: Breaking

the Scaling Relationship of Ammonia Synthesis, J. Am. Chem. Soc., 142 (2020) 17403-17412. https://doi.org/10.1021/jacs.0c06118

[22] C. Mao, L. Yu, J. Li, J. Zhao, L. Zhang, Energy-confined solar thermal ammonia synthesis with K/Ru/TiO2-xHx, Appl. Catal. B: Environ., 224 (2018) 612-620. https://doi.org/10.1016/j.apcatb.2017.11.010

[23] Y. Yang, T. Zhang, Z. Ge, Y. Lu, H. Chang, P. Xiao, R. Zhao, Y. Ma, Y. Chen, Highly enhanced stability and efficiency for atmospheric ammonia photocatalysis by hot electrons from a graphene composite catalyst with Al2O3, Carbon, 124 (2017) 72-78. https://doi.org/10.1016/j.carbon.2017.07.014

[24] Y. Peng, J. Albero, A. Franconetti, P. Concepción, H. García, Visible and NIR Light Assistance of the N2 Reduction to NH3 Catalyzed by Cs-promoted Ru Nanoparticles Supported on Strontium Titanate, ACS Catal., 12 (2022) 4938-4946. 10.1021/acscatal.2c00509

[25] S. Wang, W. Yu, S. Xu, K. Han, F. Wang, Ammonia from Photothermal N2 Hydrogenation over Ni/TiO2 Catalysts under Mild Conditions, ACS Sustain. Chem. Eng., 10 (2022) 115-123. 10.1021/acssuschemeng.1c04931

[26] M. Ravi, J.W. Makepeace, Facilitating green ammonia manufacture under milder conditions: what do heterogeneous catalyst formulations have to offer?, Chem. Sci., 13 (2022) 890-908. https://doi.org/10.1039/D1SC04734E

[27] D. Zhu, L. Zhang, R.E. Ruther, R.J. Hamers, Photo-illuminated diamond as a solid-state source of solvated electrons in water for nitrogen reduction, Nat. Mater., 12 (2013) 836-841. https://doi.org/10.1038/nmat3696

[28] Z. Li, Z. Pan, S. Cai, Z. Gao, Z. Li, R. Fu, Z. Zhao, X. Mu, L. Li, Electronic and Interface Regulation of Wurtzite Surfaces Promotes Photocatalytic Ammonia Synthesis under Visible Light Irradiation, ACS Sustain. Chem. Eng., 9 (2021) 13630-13639. https://doi.org/10.1021/acssuschemeng.1c05107

[29] M.Y. Byun, Y.E. Kim, J.H. Baek, J. Jae, M.S. Lee, Effect of surface properties of TiO2 on the performance of Pt/TiO2 catalysts for furfural hydrogenation, RSC Adv., 12 (2022) 860-868. https://doi.org/10.1039/D1RA07220J

[30] R.A. Spurr, H. Myers, Quantitative Analysis of Anatase-Rutile Mixtures with an X-Ray Diffractometer, Anal. Chem., 29 (1957) 760-762. https://doi.org/10.1021/ac60125a006

[31] B. Coşkuner Filiz, E.S. Gnanakumar, A. Martínez-Arias, R. Gengler, P. Rudolf, G. Rothenberg, N.R. Shiju, Highly Selective Hydrogenation of Levulinic Acid to γ-Valerolactone Over Ru/ZrO2 Catalysts, Catal. Letters, 147 (2017) 1744-1753. https://doi.org/10.1007/s10562-017-2049-x

[32] K.-i. Aika, K. Tamara, Ammonia Synthesis over Non-Iron Catalysts and Related Phenomena, in: A. Nielsen (Ed.) Ammonia: Catalysis and Manufacture, Springer Berlin Heidelberg, Berlin, Heidelberg, 1995, pp. 103-148.

[33] M. Kitano, Y. Inoue, Y. Yamazaki, F. Hayashi, S. Kanbara, S. Matsuishi, T. Yokoyama, S.-W. Kim, M. Hara, H. Hosono, Ammonia synthesis using a stable electride as an electron donor and reversible hydrogen store, Nat. Chem., 4 (2012) 934-940. https://doi.org/10.1038/nchem.1476

[34] H. Liu, Ammonia Synthesis Catalysts, WORLD SCIENTIFIC / CHEMICAL INDUSTRY PRESS, CHINA2011.

[35] M. Hattori, S. Iijima, T. Nakao, H. Hosono, M. Hara, Solid solution for catalytic ammonia synthesis from nitrogen and hydrogen gases at 50 °C, Nat. Commun., 11 (2020) 2001. 10.1038/s41467-020-15868-8

[36] C. Fernández, C. Sassoye, D.P. Debecker, C. Sanchez, P. Ruiz, Effect of the size and distribution of supported Ru nanoparticles on their activity in ammonia synthesis under mild reaction conditions, Appl. Catal. A: Gen., 474 (2014) 194-202. https://doi.org/10.1016/j.apcata.2013.09.039

[37] D.R. Strongin, J. Carrazza, S.R. Bare, G.A. Somorjai, The importance of C7 sites and surface roughness in the ammonia synthesis reaction over iron, J. Catal., 103 (1987) 213-215. https://doi.org/10.1016/0021-9517(87)90109-6

[38] G. Ertl, Reactions at Surfaces: From Atoms to Complexity (Nobel Lecture), Angew. Chem., Int. Ed., 47 (2008) 3524-3535. https://doi.org/10.1002/anie.200800480

[39] T. Kandemir, M.E. Schuster, A. Senyshyn, M. Behrens, R. Schlögl, The Haber–Bosch Process Revisited: On the Real Structure and Stability of "Ammonia Iron" under Working Conditions, Angew. Chem., Int. Ed., 52 (2013) 12723-12726. https://doi.org/10.1002/anie.201305812

[40] R. Harpeness, Z. Peng, X. Liu, V.G. Pol, Y. Koltypin, A. Gedanken, Controlling the agglomeration of anisotropic Ru nanoparticles by the microwave–polyol process, J. Colloid Interface Sci., 287 (2005) 678-684. https://doi.org/10.1016/j.jcis.2005.02.020

[41] T. Pakizeh, Optical absorption of nanoparticles described by an electronic local interband transition, J. Opt., 15 (2013) 025001. https://doi.org/10.1088/2040-8978/15/2/025001

[42] J.A. Creighton, D.G. Eadon, Ultraviolet–visible absorption spectra of the colloidal metallic elements, Journal of the Chemical Society, Faraday Transactions, 87 (1991) 3881-3891. 10.1039/FT9918703881

[43] J.H. Weaver, Optical properties of Rh, Pd, Ir, and Pt, Physical Review B, 11 (1975) 1416-1425. 10.1103/PhysRevB.11.1416

[44] X.-N. Guo, Z.-F. Jiao, G.-Q. Jin, X.-Y. Guo, Photocatalytic Fischer–Tropsch Synthesis on Graphene-Supported Worm-Like Ruthenium Nanostructures, ACS Catal., 5 (2015) 3836-3840. https://doi.org/10.1021/acscatal.5b00697

[45] J. Ivanez, P. Garcia-Munoz, A.M. Ruppert, N. Keller, UV-A light-assisted gas-phase formic acid decomposition on photo-thermo Ru/TiO2 catalyst, Catalysis Today, 380 (2021) 138-146. https://doi.org/10.1016/j.cattod.2021.03.020

[46] Y. Dubi, I.W. Un, Y. Sivan, Thermal effects – an alternative mechanism for plasmon-assisted photocatalysis, Chem. Sci., 11 (2020) 5017-5027. https://doi.org/10.1039/C9SC06480J

[47] X. Zhang, X. Li, M.E. Reish, D. Zhang, N.Q. Su, Y. Gutiérrez, F. Moreno, W. Yang, H.O. Everitt, J. Liu, Plasmon-Enhanced Catalysis: Distinguishing Thermal and Nonthermal Effects, Nano Lett., 18 (2018) 1714-1723. https://doi.org/10.1021/acs.nanolett.7b04776

[48] T. Gao, B.P. Jelle, Thermal Conductivity of TiO2 Nanotubes, J. Phys. Chem. C, 117 (2013) 1401-1408. 10.1021/jp3108655

[49] S. Mukherjee, F. Libisch, N. Large, O. Neumann, L.V. Brown, J. Cheng, J.B. Lassiter, E.A. Carter, P. Nordlander, N.J. Halas, Hot Electrons Do the Impossible:

Plasmon-Induced Dissociation of H2 on Au, Nano Lett., 13 (2013) 240-247. https://doi.org/10.1021/nl303940z

[50] Z. Zhang, J.T. Yates, Jr., Band Bending in Semiconductors: Chemical and Physical Consequences at Surfaces and Interfaces, Chem. Rev., 112 (2012) 5520-5551. https://doi.org/10.1021/cr3000626

Supplementary Material

Sustainable ammonia synthesis on TiO_2-based photo-thermo catalysts

Laura Valenzuela, Javier Ivanez, Nicolas Keller*

Institut de Chimie et Procédés pour l'Energie, l'Environnement et la Santé (ICPEES), CNRS, Strasbourg University, 25 rue Becquerel, 67087, Strasbourg, France.

*Corresponding author: nkeller@unistra.fr (N. Keller)

Contents:

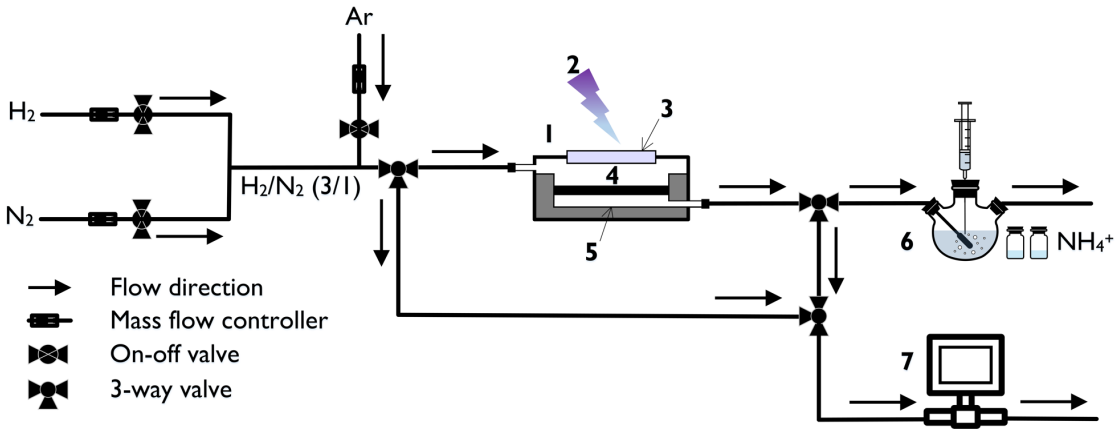

Figure S1. Scheme of the experimental setup used for photo-thermo catalytic NH_3 synthesis. **(1)** Photoreactor, **(2)** UV-A LED (λ = 365 nm, 365 mW cm^{-2}) with emission spectrum below, **(3)** quartz window, **(4)** catalyst bed (surface density of 27 mg cm^{-2}), **(5)** cartridge heater (200-350 °C), **(6)** absorption bottle (2.5 mM H_2SO_4) and **(7)** online gas microchromatograph.

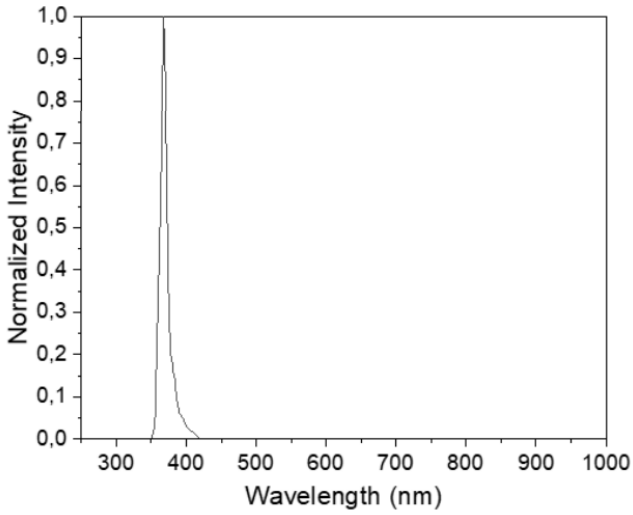

Emission spectrum of the Thorlab M365LP1 LED used for the catalytic tests.

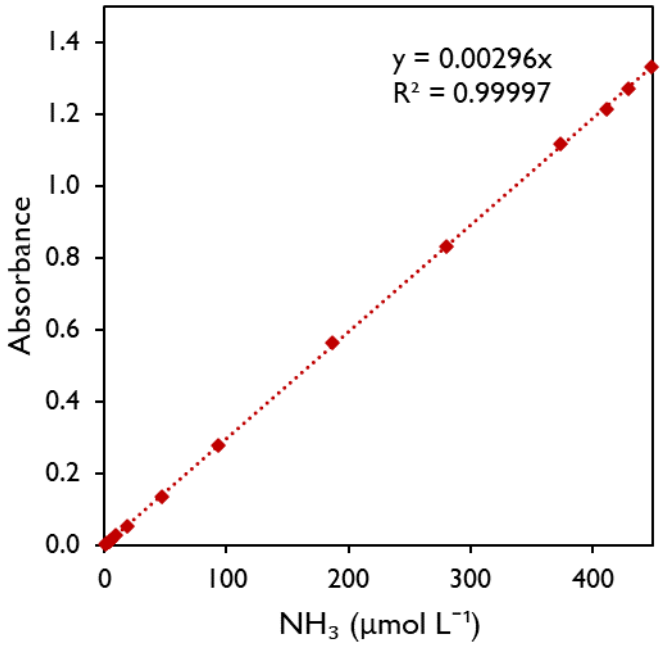

Figure S2. Calibration curve of the indophenol blue method obtained from NH_4Cl standard solutions.

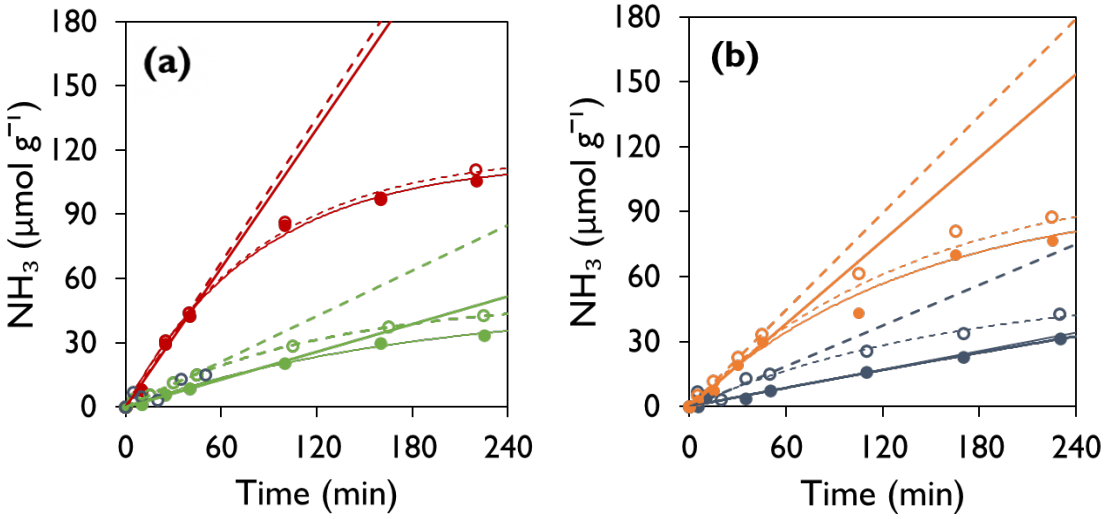

Figure S3. Time-evolution of the NH_3 concentration accumulated in the absorption bottle and deviation to the slope at origin obtained on the $5Ru/TiO_2$ catalyst, at ambient pressure in the temperature range 200-350 °C under dark thermal (—,●) and dual light/heat (---, o) conditions. Temperatures: **(a)** 250 °C (■) and 350 °C ; **(b)** 200 °C (■) and 300 °C (■).